Journal of Materials Chemistry A

ROYAL SOCIETY OF CHEMISTRY

PAPER

View Article Online
View Journal | View Issue

Cite this: *J. Mater. Chem. A*, 2020, **8**, 1865

Stabilizing n-type hetero-junctions for NiO_x based inverted planar perovskite solar cells with an efficiency of 21.6%†

Wei Chen, [ab] Guotao Pang,[c] Yecheng Zhou, [d] Yizhe Sun,[c] Fang-Zhou Liu,[b] Rui Chen,[c] Shuming Chen, [c] Aleksandra B. Djurišić *[b] and Zhubing He *[a]

The performance and stability of inverted perovskite solar cells (PSC), in particular, those with stable metal oxide hole transport layers, are limited by the instability of perovskite/electron transport layer heterojunctions. In this work, we demonstrate a successful strategy for passivating and stabilizing the perovskite/electronic transport layer n-type heterojunction in a nickel oxide based inverted planar PSC by using chemically stable inorganic $Cd_xZn_{1-x}Se_yS_{1-y}$ quantum dots (QDs). Experimental and theoretical results demonstrate that the defects/traps (unsaturated Pb^{2+} and mobile iodine ions) on perovskite surfaces can be substantially suppressed by the QDs, leading to a significant reduction of interfacial recombination and more stable n-type heterojunction. Consequently, a significant enhancement of the open-circuit voltage from 1.075 V to 1.162 V and power conversion efficiency from 19.47% to 21.63% is achieved for the QD passivated perovskite-based devices. We also demonstrate that the stabilized n-type hetero-junction results in a dramatic improvement of long-term and operational device stability. Our work demonstrates an effective and simple way to stabilize the perovskite/electron transport layer interface to develop high efficiency stable inverted planar PSCs, which will bring these devices closer to future commercial applications.

Received 11th November 2019
Accepted 23rd December 2019

DOI: 10.1039/c9ta12368g

rsc.li/materials-a

Introduction

Organic–inorganic halide perovskite materials have attracted lots of attention in recent years because of their application in optoelectronic devices, mainly driven by rapid performance improvements in halide perovskite solar cells (PSCs) and light emitting diodes.[1–3] A record power conversion efficiency (PCE) of 25.2% has been achieved for PSCs.[4] High-efficiency devices are commonly based on a conventional device structure, with TiO_2 or SnO_2 charge transport layers which often require high deposition temperatures.[2,5–8] On the other hand, planar PSCs with an inverted structure are attracting increasing attention owing to their simplified fabrication process, lower hysteresis, and good stability.[9,10] However, while the PCE of inverted planar PSCs has recently exceeded 21%,[11–13] it still lags behind the PCE of conventional structure PSCs.[14,15] Currently, the majority of high performance inverted planar PSCs use organic semiconductors, typically poly[bis(4-phenyl)(2,4,6-trimethylphenyl) amine] (PTAA), as p-type hole transport layers (HTLs).[11–13,16,17] However, due to the intrinsic chemical volatility of organic semiconductors, they usually suffer from poor stability, which hinders the commercialization process of promising inverted planar PSCs.[18] This can be potentially resolved by using highly chemical stable inorganic HTLs (such as metal oxides and carbon based semiconductors).[10,19–25]

However, the PCE of this type of device is still lower as compared with the organic counterparts.[20–24] Besides lower short circuit current density (J_{sc}), the smaller open-circuit voltage (V_{oc}) mainly contributes to lower efficiency of inverted planar PSCs with inorganic HTLs. Various approaches have been adopted to increase the efficiency of inverted PSCs, such as optimizing the perovskite composition, increasing the light absorption and the thickness of the perovskite absorber layer, and enhancing the charge transport rate.[11,17,26–28] Therefore, the optimization of charge transport layers/perovskite hetero-junctions (p-type and/or n-type) plays an important role in both device performance and stability. For n-type hetero-junctions, fullerene (C60) has been widely used as an n-type layer in inverted planar PSCs owing to its excellent electron mobility and suitable band alignment with perovskites.[29]

[a]*Department of Materials Science and Engineering, Shenzhen Key Laboratory of Full Spectral Solar Electricity Generation (FSSEG), Southern University of Science and Technology, No. 1088, Xueyuan Rd., Shenzhen, Guangdong, 518055, P. R. China. E-mail: hezb@sustech.edu.cn*

[b]*Department of Physics, The University of Hong Kong, Pokfulam, Hong Kong SAR. E-mail: dalek@hku.hk*

[c]*Department of Electrical and Electronic Engineering, Southern University of Science and Technology, No. 1088, Xueyuan Rd., Shenzhen, Guangdong, 518055, P. R. China*

[d]*Department of Materials Science and Engineering, Sun Yat-sen University, 135, Xingang West road, Guangzhou, 510275, P. R. China*

† Electronic supplementary information (ESI) available. See DOI: 10.1039/c9ta12368g

However, despite its advantages, devices with C60 exhibit lower efficiency due to interfacial recombination and inferior stability due to easy cross-diffusion of halide and metal ions from the perovskite and metal electrode layers, respectively.[30] As a result, stabilizing the n-type hetero-junction becomes critical for achieving both stable and efficient inverted PSCs. Efforts such as surface passivation,[17,27,31,32] bulk heterojunction engineering[26] and secondary growth (SSG) techniques[11] have been made to stabilize the n-type hetero-junction and reduce the nonradiative recombination. To further enhance the device stability by preventing ion diffusion at the n-type hetero-junction, inorganic quantum dots (QDs), especially metal chalcogen semiconductor QDs (*e.g.* CdS/Se and CdSe/ZnS), have attracted increasing attention owing to their chemical compatibility with perovskites, chemical stability, well matched crystal structure, and excellent optoelectronic properties.[33–36] However, the reports of QD application in PSCs mainly investigated conventional structure devices,[37–43] as hole transporting layers,[37,41] interfacial layers[38,39,42,43] or seed layers for improving the crystallinity of the perovskite.[40] Due to differences in the architecture (materials used) and behaviour of conventional and inverted devices, the mechanisms responsible for the improved performance do not necessarily directly translate to inverted devices. For example, the reduction of hysteresis due to faster hole extraction in conventional devices[38] is not applicable to inverted devices which do not exhibit significant hysteresis, and QDs are placed between the perovskite and electron transport layer. The reports on the use of chalcogenide QDs in inverted structures have been scarce.[36,44,45] While it has been demonstrated that the use of chalcogenide QDs can lead to performance improvements, the achieved efficiencies were relatively low and need to be increased.[36,44,45] Therefore, QDs with a suitable band gap have the potential to stabilize the perovskite/C60 hetero-junction in inverted planar PSCs, enhancing both the stability and performance of devices.

Herein, we employed $Cd_xZn_{1-x}Se_yS_{1-y}$ alloyed QDs to stabilize the n-type hetero-junction in NiO_x HTL based inverted planar PSCs. The QDs are used as an interface modification layer to passivate the defects and stabilize the interface between the perovskite and C60, rather than as a charge transport layer. The commercially available QDs show high PL quantum yields (>85%),[34] which guarantees that they have low defects/trap density both at the surfaces and in the bulk of QDs which makes them promising for the passivation of perovskite surfaces. Moreover, the suitable energy level alignment of QDs with perovskite could further enhance the electron extraction rate at the n-type heterojunction. In addition, QDs can be easily dissolved in nonpolar solvents such as toluene, octane and chlorobenzene, which ensures that the deposition process of QDs is compatible with perovskite films and does not damage the perovskite layers. We demonstrate that a stabilized n-type hetero-junction induced by QDs can effectively passivate defects at perovskite surfaces, resulting in a significant photovoltaic performance enhancement, with the increase of V_{oc} from 1.075 V to 1.162 V, and the PCE from 19.47% up to 21.6%. Moreover, a stabilized n-type hetero-junction also improves substantially both long-term and operational device stability.

Results and discussion

As shown in the schematic diagram of the architecture of inverted planar PSCs in Fig. 1a, the inverted planar perovskite solar cells employ the following structure ITO/NiO_x/perovskites (with and without QD passivation)/C60/BCP/Ag, where NiO_x and C60 are p and n-type selective layers, respectively. Low temperature processed NiO_x nanoparticle HTLs were prepared according to our previous reports (see Experimental details in the ESI†).[46,47] Mixed cation perovskites (denoted as CsFAMA) were fabricated by one step antisolvent methods (see Experimental details in the ESI†).[21] Before depositing C60 ETLs, surface passivation of perovskite films was achieved by spin coating a commercial QD solution (Cat. no. CdSe-525-25, Mesolight Inc.) with various concentrations (see Experimental details in the ESI†). TEM images show the uniform size distribution (~8 nm) and high crystallinity of the QDs (Fig. S1, ESI†). The absorption spectrum of QDs demonstrates that the absorption edge is located at ~540 nm, corresponding to an optical band gap of ~2.3 eV, consistent with the strong green photoluminescence (PL) from QD solution under excitation (Fig. S2, ESI†). The intense luminescence of QDs (PLQY > 85%) demonstrates the low bulk and/or surface defect/trap state density present in the QDs,[34] which makes them promising candidates for passivating and stabilizing the interfacial traps after depositing QDs on perovskites. In addition, the valence band and conduction band values of QDs are ~6.2 eV and 3.9 eV, respectively.[34] This suitable conduction band and valence band values enable effective electron extraction from the perovskite to QDs and sufficient hole blocking.[36] SEM images of the perovskite films with and without QD interfacial layers are shown in Fig. S3, ESI.† We can observe that after spin-coating QD solution, the perovskite films are covered uniformly by QDs.

It is well recognized that Pb^{2+} has strong binding with S/Se to form PbS/PbSe quantum dots. Previous reports demonstrated that PbS/PbSe QDs can effectively protect the 3D perovskite by forming a QD matrix surrounding the perovskite.[48,49] In our case, we speculate that the S/Se elements in the QDs could effectively coordinate with unsaturated Pb^{2+} defect sites, which can protect and stabilize the perovskite surface and then suppress interfacial recombination and facilitate electron extraction (Fig. 1a). Moreover, mobile iodine ions might be effectively captured or stabilized by Zn/Cd in the QDs. To confirm our hypothesis, we performed high resolution X-ray photoelectron spectroscopy (XPS) analysis for perovskite films with and without QD passivation as well as pure QD film. From the XPS data shown in Fig. 1b, we can observe a shift of core levels of Pb 4f to lower energy (~0.29 eV) in the QD passivated perovskite samples, which indicates a change in the chemical environment of Pb^{2+}.[50] Furthermore, we can observe the disappearance of the lower intensity feature (~1.8 eV lower than the main doublet) which corresponds to metallic Pb^0 4f.[51] The observed changes in the XPS spectra are consistent with the interaction between S/Se in the QDs and unsaturated Pb^{2+} ions, indicating possible defect passivation in the perovskite film.

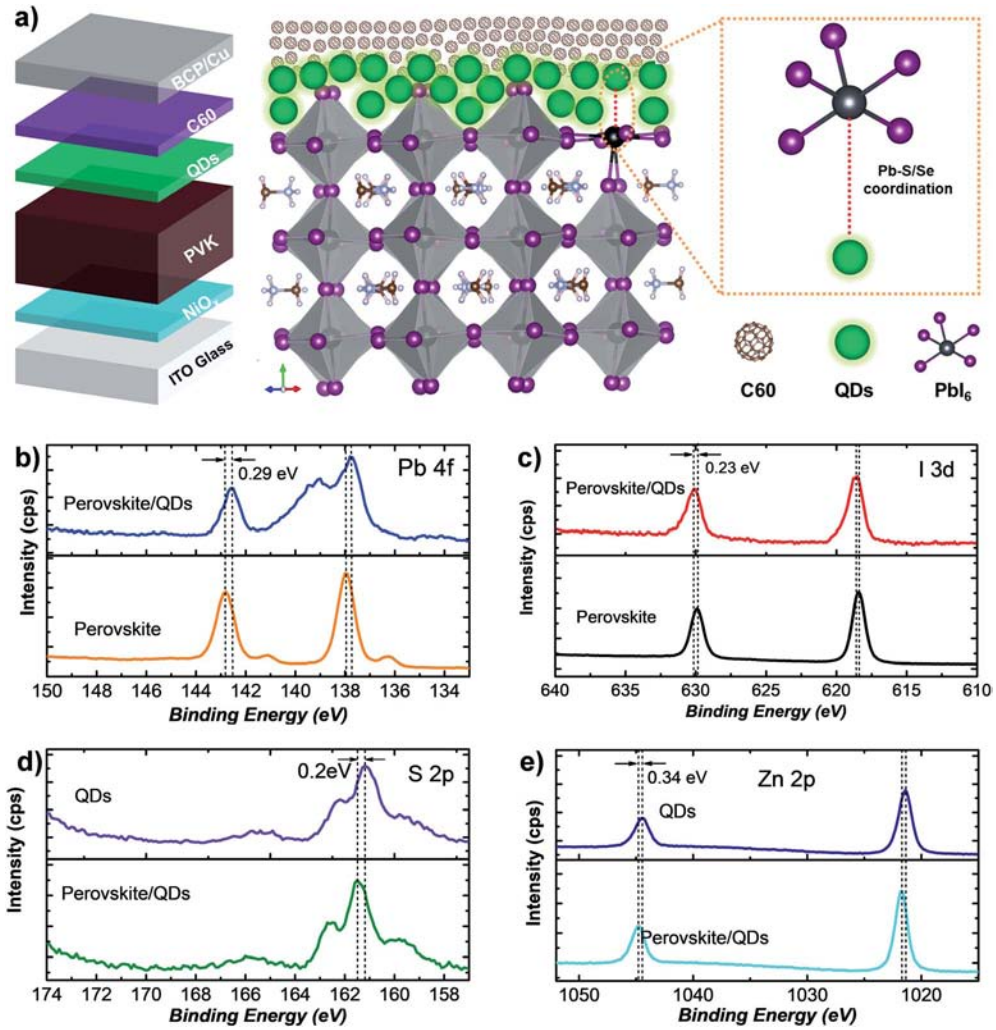

Fig. 1 (a) Schematic diagram of the inverted planar perovskite solar cell (PSC) architecture investigated in this work. Enlarged dashed frame shows the interfacial details of perovskite/QDs/C60, where the S or Se in QDs could effectively coordinate with unsaturated Pb defects/traps (note that the sizes of QDs, C60 and perovskite in the schematic diagram are not on real scale); (b to e) high resolution X-ray photoelectron spectroscopy (XPS) profiles of Pb (b), I (c), S (d) and Zn (e) in the pure perovskite, pure QD and perovskite/QD samples.

Moreover, the shift of core levels of I 3d to higher energy (~0.23 eV) might indicate the coordination between I^- in perovskite and metals (Zn/Cd) in QDs (Fig. 1c). This is also consistent with the observed changes in the XPS peaks of S/Se and Zn/Cd 2p core levels of QDs on perovskite,[50] as shown in Fig. 1d, e and S4, ESI.† The XPS results indicate a strong interaction between perovskite and QDs, which suggests that effective defect passivation can be achieved in the perovskite/QD system.

To further elucidate the effect of QDs on the suppression of surface defects in perovskite, we performed density functional theory (DFT) simulations to calculate the formation energies of iodine (I) and lead (Pb) vacancies on the surface of the pure perovskite, and that on the surfaces passivated with QDs. The unit cell structures of the pure perovskites are shown in Fig. S5, ESI.† Fig. 2a and b present the optimal model structures of the QD modified perovskite with excess I and Pb, respectively. To simplify the unit cell structure in DFT calculation, we used cadmium sulfide (CdS) to imitate the CdZnSeS QDs in the unit cell structure. The formation energy of I vacancies increases from 1.17 eV for the pristine perovskite to 1.95 eV for the QD modified perovskite. A significant increase of formation energy of Pb vacancies is also observed after QD modification of perovskite (Fig. 2c). Our calculation results indicate that the modification with QDs prevents the formation of I and Pb vacancies at the surface and are consistent with previous XPS results.

The device lateral morphology has also been examined by transmission electron microscopy (TEM), as shown in Fig. 3. Low magnification TEM shows clearly each layer in our inverted planar PSCs, including the QD passivation layers. To specify the n-type hetero-junction (perovskite/QDs/C60) region, we enlarge the frame region by HRTEM. The images of the QDs/C60 layers show that C60 has partially diffused into the QD layers to form hybrid ETLs due to the small size of single C60 nanoparticles (6.5–7 Å).[52] QDs with similar sizes to those determined from the TEM images of the pure QDs

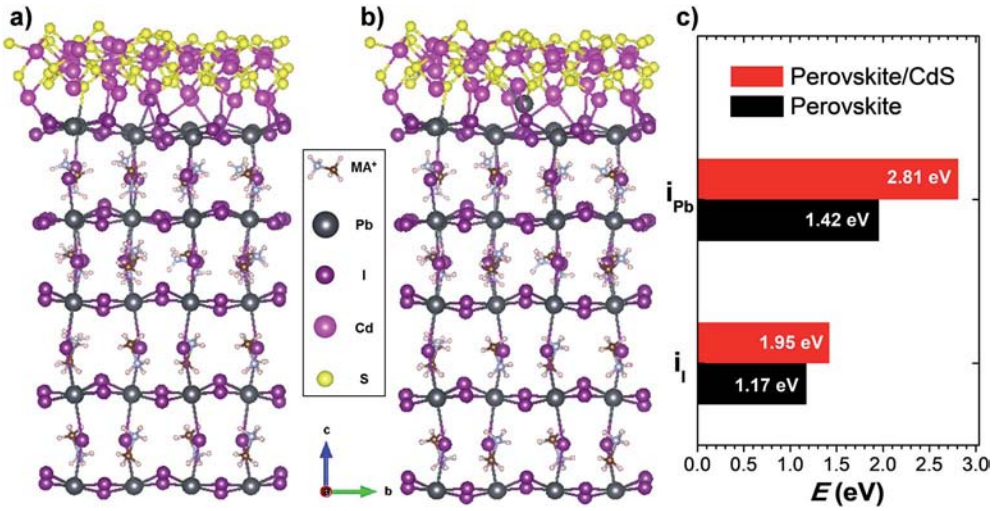

Fig. 2 Optimized structures of a perovskite/CdS unit cell with excess iodine (a) and lead (b) at the perovskite/CdS interface; (c) formation energy of surface iodine vacancies (i_I) and lead vacancies (i_{Pb}) in the pure perovskite and in the CdS modified perovskite surfaces.

(Fig. S1, ESI†) can be clearly detected in hybrid layers in the HRTEM image. The average thickness of the QD layers was calculated to be ~20 nm. Furthermore, EDS mapping in HAADF mode is consistent with the expected device composition and it is in agreement with TOF-SIMS profiles of the devices shown in Fig. S6, ESI.†

To investigate the impact of QD passivation on the device performances, the photovoltaic performance of the devices was investigated in detail, and the obtained results are presented in Fig. 4 and summarized at Table 1. We can observe that there is an optimal concentration of QDs which results in the largest enhancement of device performance. The optimal device efficiency is enhanced from 19.47% (short circuit current density (J_{sc}) of 22.73 mA cm^{-2}, open circuit voltage (V_{oc}) of 1.075 V, and fill factor (FF) of 79.7%) for the control device to 21.63% (J_{sc} of 22.88 mA cm^{-2}, V_{oc} of 1.162 V, and FF of 81.4%) for the optimal QD passivated device. Both the control and QD passivated devices (Fig. 4b and S7, ESI†) exhibit negligible hysteresis, which is common for inverted planar devices with fullerene ETLs.[24] Stabilized power output (SPO) for both devices measured under fixed bias (V_{mpp}) over 500 s further demonstrates the negligible hysteresis behavior, as plotted in Fig. 4c.

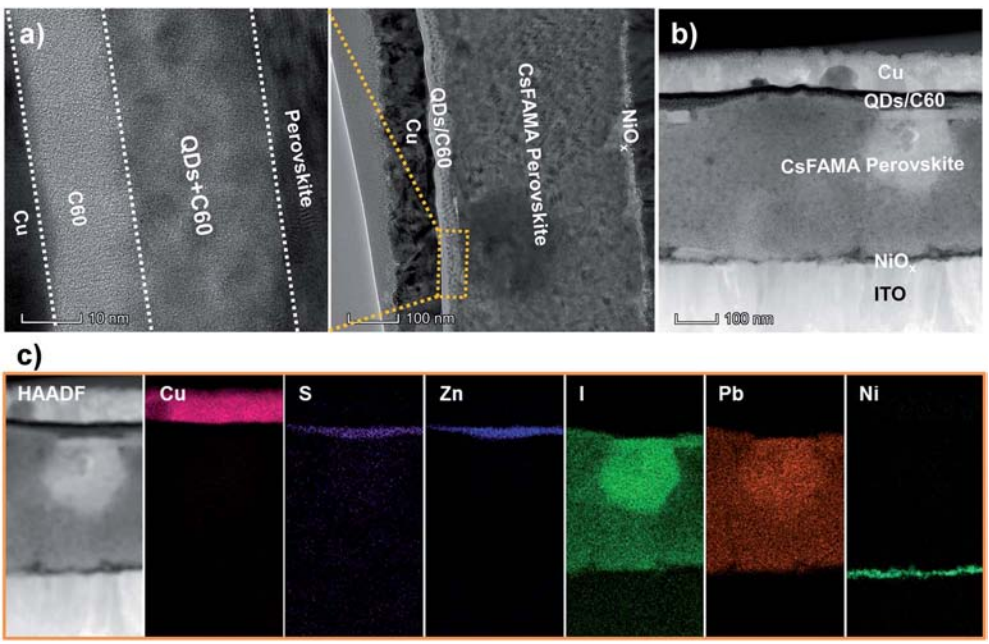

Fig. 3 (a) Transmission electron microscopy (TEM) and high resolution TEM images of cross sectional morphologies for a complete device and C60/Perovskite interface; (b) scanning transmission electron microscopy (STEM) images of the cross sectional morphologies in HAADF mode; (c) the corresponding energy-dispersive X-ray spectroscopy (EDS) mappings of various elements in the devices.

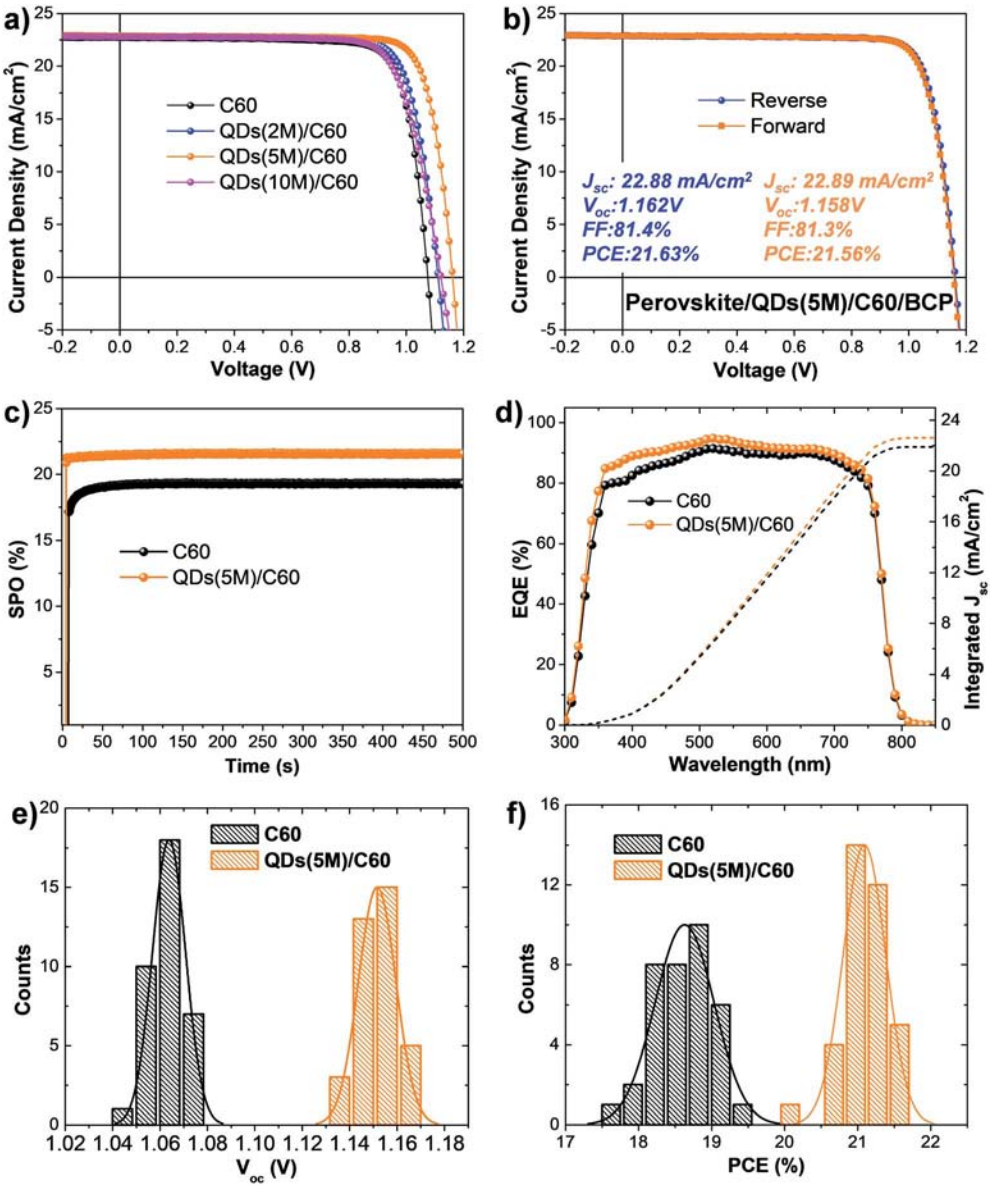

Fig. 4 (a) Current–voltage (I–V) characteristics of the inverted planar PSCs with C60 and QDs/C60 hybrid ETLs (the device area is 10 mm^2, defined by an optical aperture); (b) I–V hysteresis behaviours of the optimal PSCs with QD (5 mg ml^{-1} (M)) hybrid ETLs; (c) steady power output of the optimal PSCs with C60 and QDs(5M)/C60 hybrid ETLs; (d) EQE spectra of the optimal PSCs with C60 and QDs(5M)/C60 hybrid ETLs; (e and f) statistics of the V_{oc} (e) and PCE (f) for the PSCs with C60 and QDs(5M)/C60 hybrid ETLs.

The SPO efficiencies were 19.23% and 21.52% for control and QD passivated devices, respectively, consistent with the results from I–V scan. From the comparison of device performance with and without QD stabilization, we can observe that QD passivation results in a small increase of J_{sc}, but a significant increase of V_{oc} (~100 mV) and FF, resulting in a significant enhancement of PCE. From the performance statistics shown in Fig. 4e and f, it is clear that performance enhancement, in particular in the case of V_{oc}, is larger than the experimental variation in the performance of different devices. An increase in V_{oc} is

Table 1 Summary of the photovoltaic performance parameters of the inverted planar PSCs with and without QD passivation

Devices	Scan direction	V_{oc} (V)	J_{sc} (mA cm^{-2})	FF (%)	PCE (%)
C60	Reverse	1.075	22.73	79.7	19.47
	Forward	1.074	22.72	79.1	19.30
QDs(5M)/C60	Reverse	1.162	22.88	81.4	21.63
	Forward	1.158	22.89	81.3	21.56

consistent with passivation of defects,[17] which can occur by successful coordination of unsaturated Pb^{2+} ions, in agreement with XPS results. We can also observe that the integrated J_{sc} from external quantum efficiency (EQE) spectra is in good agreement with the measured J_{sc} values from I–V curves (Fig. 4d). Furthermore, the shape of the EQE curves with and without QDs indicates additional enhancement in the spectral region <550 nm, which may indicate that the QDs absorb the light reflected from the rear silver electrode film and possible irradiative recombination of electron–hole pairs in perovskite. That is consistent with light absorption by QDs and charge transfer, as well as enhanced electron extraction by QDs.[36,43]

To investigate the reason for the performance improvement in devices after n-type hetero-junction stabilization with QDs, detailed characterization of the PSCs with and without QDs was conducted. Time resolved photoluminescence (TRPL) spectra are shown in Fig. 5a, while the fitting results are summarized in Table 2. Photoluminescence quenching and PL lifetime are affected both by carrier extraction and carrier trapping at the b-type hetero-junction.[53] The PL decay can be commonly described by a bi-exponential decay, consisting of a fast and a slow decay component.[53–55] Significant shortening of the fast decay component in the presence of an ETL is an indicator of efficient charge extraction.[12,17,27] On the other hand, we can

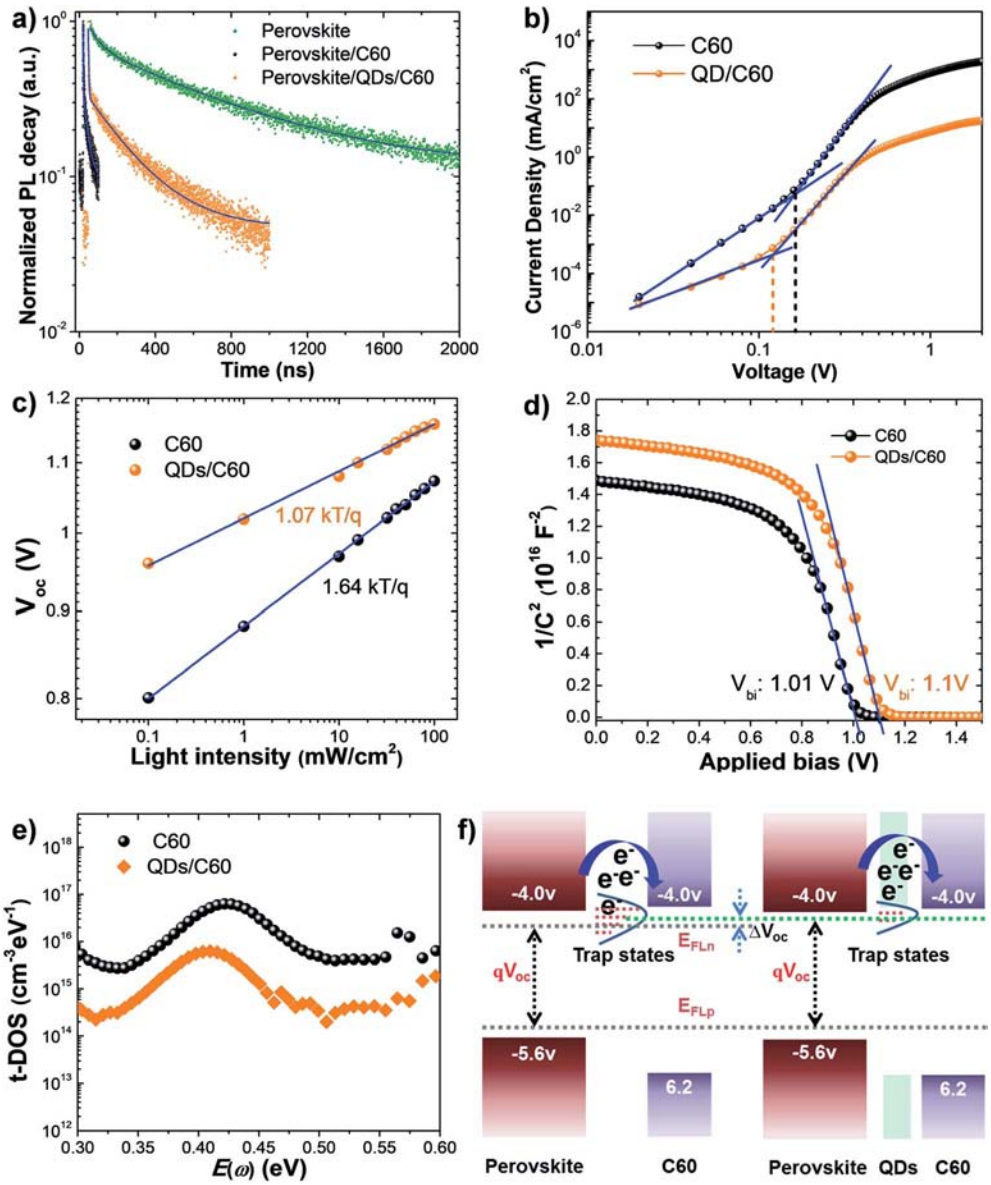

Fig. 5 (a) Photoluminescence (PL) decay spectra of the perovskite films with and without QD passivation under 405 nm excitation from the perovskite side; (b) I–V characteristics of the electron only devices with the structure of ITO/SnO_2/CsFAMA perovskites/with or without QDs/C60/BCP/Ag; (c) open circuit voltage (V_{oc}) as a function of illumination intensity for the PSCs with and without QD stabilization; (d) Mott–Schottky characteristics of the PSCs with and without QD stabilization; (e) trap density of state (t-DOS) characteristics of the PSCs with and without QD stabilization; (f) schematic illustration of the band alignments and trap states at the perovskite/QDs/C60 n-type hetero-junction.

Table 2 Summary of the charge carrier dynamics by fitting the PL decay curves

Samples	A_1 (%)	τ_1 [ns]	A_2 (%)	τ_2 [ns]	Weighted average τ [ns]
Perovskite (PVK)	31	56.0	69	656.1	633.9
PVK/C60	65	1.6	35	25.0	22.5
PVK/QDs/C60	57	2.7	43	215.8	212.3

observe a significant increase in the slow decay component for the QD-stabilized perovskite, which indicates successful passivation of interfacial defects.[12] Consequently, the trap-assisted recombination can be effectively suppressed after QD stabilization, which could dramatically increase V_{oc}.[11,32]

To further investigate the trap passivation by QDs, we examined electron transport using electron-only devices, as shown in Fig. 5b.[54] From determining the trap-filled limit voltage V_{TFL} as the point where the I–V curve changes from the ohmic (I–V) to the trap-filled limit regime (I–$V^{n>3}$).[21] Then the trap density N_t can be determined as: $N_t = \frac{2\varepsilon\varepsilon_0 V_{TFL}}{eL^2}$, where e is the elementary charge of the electron, L is the perovskite film thickness, ε is the relative dielectric constant of perovskite ($\varepsilon = \sim 30$), ε_0 is the vacuum permittivity, and N_t is the trap-state density. For the control device, the N_t was calculated to be 2.4×10^{15}. After QD passivation, the N_t of the optimal devices was reduced to 7.3×10^{14}. This indicates that the apparent suppression of the trap states in the perovskite/C60 heterojunction can be achieved with QD stabilization, consistent

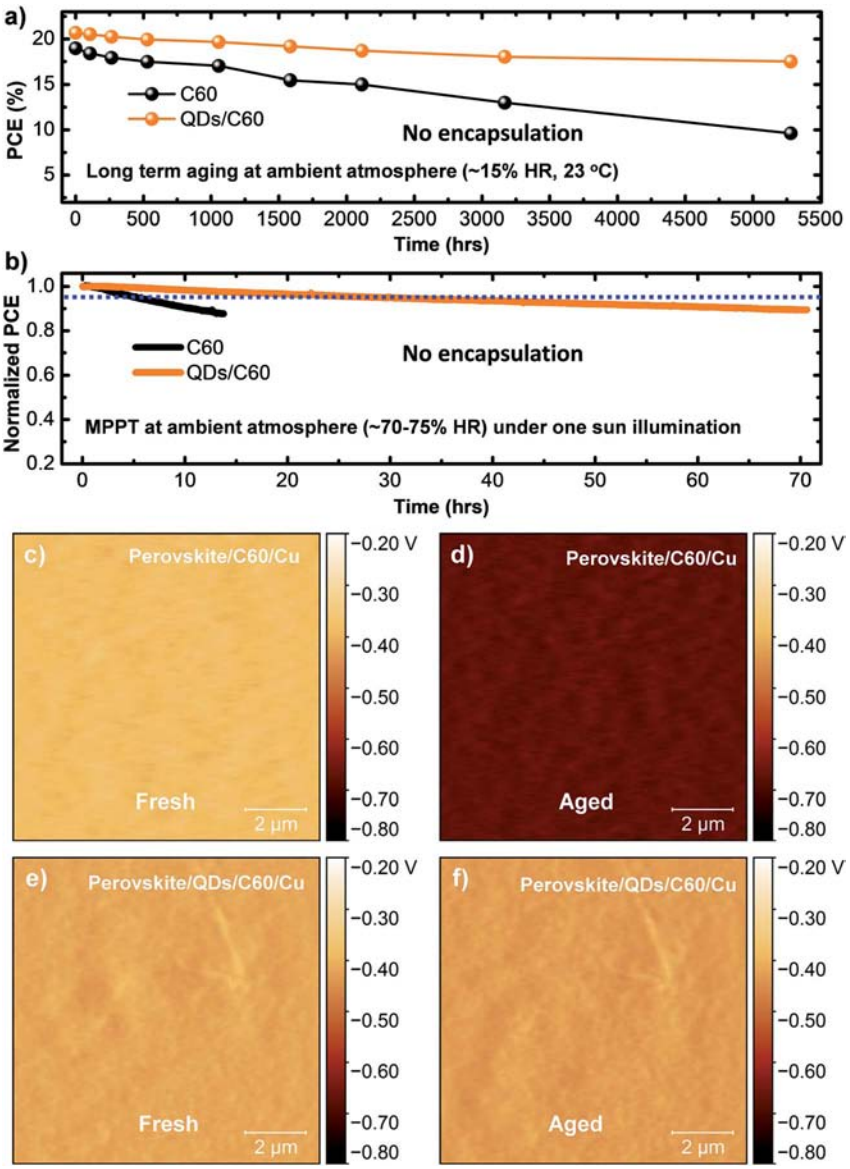

Fig. 6 (a) Long term stability tests for the PSCs with and without QD passivation stored in a dry box (~15% HR, 23 °C) in the dark; (b) accelerated operational stability evaluation for the PSCs with and without QD passivation under continuous light illumination in an ambient environment (~70–75% HR) at maximum power point (MMP) tracking; surface potential profiles of fresh (c) and aged (d) perovskite/C60/Cu control devices and fresh (e) and aged (f) perovskite/QDs/C60/Cu optimal devices measured by scanning Kelvin probe microscopy (SKPM).

with photovoltaic performance and TRPL results. From the V_{oc} dependence on the light intensity (Fig. 5c), we can observe that the slope is 1.64 kT/q without QDs and 1.07 kT/q with QDs. When the slope is approaching one kT/q, it means the reduced possibility of trap-assisted recombination.[55] Therefore, the slope reduction also confirms the successful passivation of interface defects by QDs. The interfacial defects were also characterized by C–V measurements, and the resulting Mott–Schottky plots and estimated trap density of states[56–58] are shown in Fig. 5d and e, while the schematic diagram of the band alignment and trap states is shown in Fig. 5f. The obtained trap density is significantly lower in PSCs with QD passivation, in agreement with other measurements. It is expected that the trap states in the pure C60 control devices would capture the photo-generated electrons and prevent partial electron transfer from perovskite to the ETL, induce large interfacial recombination, and finally cause large V_{oc} deficits.[31,32] After passivation with QDs, the reduced trap assisted recombination can result in an upward shift of the n-type quasi Fermi level (E_{FLn}) and then narrow the V_{oc} deficits (ΔV_{oc}), resulting in a significant improvement of photovoltages and device performance.[16]

Finally, we also investigated the effect of passivation and stabilization of n-type hetero-junctions with QDs on device stability. We can observe that the water contact angle is obvious higher for QD passivated perovskite films compared to pure perovskites, as shown in Fig. S8a and b.† Increased hydrophobicity is expected to result in a lower rate of penetration of moisture into the perovskite layer. Indeed, we can observe a significant improvement in device long term stability for storage in the dark and low moisture environments (~15% RH). As illustrated in Fig. 6a, the QD passivated devices maintain over 80% of the initial performance after over 5000 hours of aging, demonstrating significantly improved device stability compared to the control device (~60%). To evaluate the operational stability of our device after n-type hetero-junction stabilization, accelerated aging tests of the non-encapsulated devices were performed with maximum power point (MPP) tracking under constant illumination and a high humidity environment (no temperature control, 70–75% RH). We can observe from Fig. 6b that the accelerated degradation rate (~3.7% per hour) for the QD passivated device is much lower than that of the control one (~28% per hour). In addition to increased hydrophobicity of the perovskite/QDs/C60 hetero-junction, the passivation of interfacial defects by chalcogen atoms in QDs also likely contributes to improved stability, particularly under light soaking, since it is expected to retard ion migration, slow down the interfacial degradation, and consequently improve the device stability.[36,59] we can confirm this by exploring the surface potential changes of the n-type hetero-junction by scanning Kelvin probe microscopy (SKPM) measurements. We fabricated perovskite/with or without QDs/C60/Cu (10 nm) samples for the SKPM measurements. Thin layers of 10 nm electrodes were evaporated to imitate the real device architecture. The samples were aged in an ambient atmosphere with a white LED lamp (~40 mW cm^{-2}) for 10 h. As shown in Fig. S9, ESI,† the surface morphology of both n-type hetero-junctions before and after aging has almost no change, while the surface potential for the aged perovskite/C60/Cu control device apparently decreases as compared with the fresh one (Fig. 6c and d), indicating the instability of the perovskite/C60 heterojunction after light soaking. In contrast, we can observe small changes of the surface potential for the perovskite/QDs/C60/Cu device before and after aging (Fig. 6e and f). From SKPM results, we can conclude that the QDs can effectively stabilize the perovskite/C60 hetero-junction to improve the device long-term and operational stabilities.

Conclusion

In summary, we have demonstrated that the interfacial defects at a perovskite/C60 n-type hetero-junction in a NiO_x HTL based inverted planar PSC can be effectively stabilized and passivated with commercially available CdZnSeS QDs. The formation of a more stable hybrid perovskite/QDs/C60 n-type hetero-junction significantly suppresses the interfacial recombination, resulting in a substantial increase of V_{oc} from 1.075 V to 1.162 V and a significant increase of PCE from 19.47% to 21.63%. Both V_{oc} and PCE in this work are higher than previously reported record values for NiO_x HTL based inverted planar PSCs. Detailed XPS characterizations verifies that S/Se elements in the QDs can coordinate with unsaturated Pb^{2+} on the perovskite surface and hence effectively stabilize the n-type hetero-junction, in agreement with the evidence for reduced trap state density at the perovskite/QDs/C60 hetero-junction obtained from comprehensive optical and electrical characterization. Moreover, defect passivation, reduced ion migration, and increased hydrophobicity of the QDs/C60 ETL also result in a significant improvement of the device operational stability under continuous light soaking. This work improves our understanding of the direct relationship between V_{oc} and the n-type hetero-junction in inverted planar PSCs, and also paves an effective way to modulate that hetero-junction for developing highly efficient and stable NiO_x HTL based inverted planar PSCs, which would provide a solution for future commercialization of perovskite photovoltaics.

Conflicts of interest

There are no conflicts to declare.

Acknowledgements

This work is supported by the National Natural Science Foundation of China (NSFC) (No. 61775091), National Key Research Project MOST (No. 2016YFA0202400), Shenzhen Key Laboratory Project (No. ZDSYS201602261933302) and Natural Science Foundation of Shenzhen Innovation Committee (No. JCYJ20180504165851864 and JCYJ20170818141216288). The support from the Seed Funding for Strategic Interdisciplinary Research Scheme of the University of Hong Kong and RGC GRF grants 15204515 and 15246816 is also acknowledged. The authors thank the Materials Characterization and Preparation

Center (MCPC) and the Pico Center of SUSTech for some characterization in this work.

Notes and references

1 M. He, D. Zheng, M. Wang, C. Lin and Z. Lin, *J. Mater. Chem. A*, 2014, **2**, 5994.
2 A. K. Jena, A. Kulkarni and T. Miyasaka, *Chem. Rev.*, 2019, **119**, 3036–3103.
3 N. Wang, L. Cheng, R. Ge, S. Zhang, Y. Miao, W. Zou, C. Yi, Y. Sun, Y. Cao, R. Yang, Y. Wei, Q. Guo, Y. Ke, M. Yu, Y. Jin, Y. Liu, Q. Ding, D. Di, L. Yang, G. Xing, H. Tian, C. Jin, F. Gao, R. H. Friend, J. Wang and W. Huang, *Nat. Photonics*, 2016, **10**, 699–704, DOI: 10.1038/nphoton.2016.185.
4 M. A. Green, E. D. Dunlop, D. H. Levi, J. Hohl-Ebinger, M. Yoshita and A. W. Y. Ho-Baillie, *Prog. Photovoltaics*, 2019, **27**, 565–575.
5 Q. Lin, A. Armin, P. L. Burn and P. Meredith, *Acc. Chem. Res.*, 2016, **49**, 545–553.
6 Y. Rong, Y. Hu, A. Mei, H. Tan, M. I. Saidaminov, S. I. Seok, M. D. McGehee, E. H. Sargent and H. Han, *Science*, 2018, **361**, eaat8235.
7 P. Gao, M. Gratzel and M. K. Nazeeruddin, *Energy Environ. Sci.*, 2014, **7**, 2448–2463.
8 Z. Xiao, Z. Song and Y. Yan, *Adv. Mater.*, 2019, e1803792, DOI: 10.1002/adma.201803792.
9 L. Meng, J. You, T. F. Guo and Y. Yang, *Acc. Chem. Res.*, 2016, **49**, 155–165.
10 S. Bai, P. Da, C. Li, Z. Wang, Z. Yuan, F. Fu, M. Kawecki, X. Liu, N. Sakai, J. T. Wang, S. Huettner, S. Buecheler, M. Fahlman, F. Gao and H. J. Snaith, *Nature*, 2019, **571**, 245–250.
11 D. Luo, W. Yang, Z. Wang, A. Sadhanala, Q. Hu, R. Su, R. Shivanna, G. F. Trindade, J. F. Watts, Z. Xu, T. Liu, K. Chen, F. Ye, P. Wu, L. Zhao, J. Wu, Y. Tu, Y. Zhang, X. Yang, W. Zhang, R. H. Friend, Q. Gong, H. J. Snaith and R. Zhu, *Science*, 2018, **360**, 1442–1446.
12 M. Stolterfoht, C. M. Wolff, J. A. Marquez, S. S. Zhang, C. J. Hages, D. Rothhardt, S. Albrecht, P. L. Burn, P. Meredith, T. Unold and D. Neher, *Nat. Energy*, 2018, **3**, 847–854.
13 W. Q. Wu, Z. Yang, P. N. Rudd, Y. Shao, X. Dai, H. Wei, J. Zhao, Y. Fang, Q. Wang, Y. Liu, Y. Deng, X. Xiao, Y. Feng and J. Huang, *Sci. Adv.*, 2019, **5**, eaav8925.
14 Q. Jiang, Y. Zhao, X. Zhang, X. Yang, Y. Chen, Z. Chu, Q. Ye, X. Li, Z. Yin and J. You, *Nat. Photonics*, 2019, **13**, 460–466.
15 M. Kim, G. H. Kim, T. K. Lee, I. W. Choi, H. W. Choi, Y. Jo, Y. J. Yoon, J. W. Kim, J. Lee, D. Huh, H. Lee, S. K. Kwak, J. Y. Kim and D. S. Kim, *Joule*, 2019, **3**, 2179–2192.
16 X. P. Zheng, J. Troughton, N. Gasparini, Y. B. Lin, M. Y. Wei, Y. Hou, J. K. Liu, K. P. Song, Z. L. Chen, C. Yang, B. Turedi, A. Y. Alsalloum, J. Pan, J. Chen, A. A. Zhumekenov, T. D. Anthopoulos, Y. Han, D. Baran, O. F. Mohammed, E. H. Sargent and O. M. Bakr, *Joule*, 2019, **3**, 1963–1976.
17 X. Zheng, B. Chen, J. Dai, Y. Fang, Y. Bai, Y. Lin, H. Wei, X. C. Zeng and J. Huang, *Nat. Energy*, 2017, **2**, 17102.
18 M. B. Islam, M. Yanagida, Y. Shirai, Y. Nabetani and K. Miyano, *Sol. Energy Mater. Sol. Cells*, 2019, **195**, 323–329.
19 D. Ouyang, Z. Huang and W. C. H. Choy, *Adv. Funct. Mater.*, 2019, **29**, 1804660.
20 W. Chen, Y. Zhou, L. Wang, Y. Wu, B. Tu, B. Yu, F. Liu, H. W. Tam, G. Wang, A. B. Djurišić, L. Huang and Z. He, *Adv. Mater.*, 2018, **30**, 1800515.
21 W. Chen, Y. Zhou, G. Chen, Y. Wu, B. Tu, F. Z. Liu, L. Huang, A. M. C. Ng, A. B. Djurišić and Z. He, *Adv. Energy Mater.*, 2019, **9**, 1803872.
22 K. Yao, S. Leng, Z. Liu, L. Fei, Y. Chen, S. Li, N. Zhou, J. Zhang, Y.-X. Xu, L. Zhou, H. Huang and A. K. Y. Jen, *Joule*, 2019, **3**, 417–431.
23 W. Chen, Y. Wu, Y. Yue, J. Liu, W. Zhang, X. Yang, H. Chen, E. Bi, I. Ashraful, M. Gratzel and L. Han, *Science*, 2015, **350**, 944–948.
24 Y. Hou, W. Chen, D. Baran, T. Stubhan, N. A. Luechinger, B. Hartmeier, M. Richter, J. Min, S. Chen, C. O. Quiroz, N. Li, H. Zhang, T. Heumueller, G. J. Matt, A. Osvet, K. Forberich, Z. G. Zhang, Y. Li, B. Winter, P. Schweizer, E. Spiecker and C. J. Brabec, *Adv. Mater.*, 2016, **28**, 5112–5120.
25 X. T. Yin, Y. X. Guo, H. X. Xie, W. X. Que and L. B. Kong, *Sol. RRL*, 2019, **3**, 1900001.
26 Y. Wu, X. Yang, W. Chen, Y. Yue, M. Cai, F. Xie, E. Bi, A. Islam and L. Han, *Nat. Energy*, 2016, **1**, 16148.
27 W. Chen, Y. Wang, G. Pang, C. W. Koh, A. B. Djurišić, Y. Wu, B. Tu, F. z. Liu, R. Chen, H. Y. Woo, X. Guo and Z. He, *Adv. Funct. Mater.*, 2019, **29**, 1808855.
28 Z. Liu, L. Krückemeier, B. Krogmeier, B. Klingebiel, J. A. Márquez, S. Levcenko, S. Öz, S. Mathur, U. Rau, T. Unold and T. Kirchartz, *ACS Energy Lett.*, 2018, 110–117, DOI: 10.1021/acsenergylett.8b01906.
29 L.-L. Deng, S.-Y. Xie and F. Gao, *Adv. Electron. Mater.*, 2017, 1700435, DOI: 10.1002/aelm.201700435.
30 A. F. Akbulatov, L. A. Frolova, M. P. Griffin, I. R. Gearba, A. Dolocan, D. A. Vanden Bout, S. Tsarev, E. A. Katz, A. F. Shestakov, K. J. Stevenson and P. A. Troshin, *Adv. Energy Mater.*, 2017, **7**, 1700476.
31 Q. Wang, Q. Dong, T. Li, A. Gruverman and J. Huang, *Adv. Mater.*, 2016, **28**, 6734–6739.
32 C. M. Wolff, F. Zu, A. Paulke, L. P. Toro, N. Koch and D. Neher, *Adv. Mater.*, 2017, **29**, 1700159.
33 X. Dai, Z. Zhang, Y. Jin, Y. Niu, H. Cao, X. Liang, L. Chen, J. Wang and X. Peng, *Nature*, 2014, **515**, 96–99.
34 Y. Sun, W. Chen, Y. Wu, Z. He, S. Zhang and S. Chen, *Nanoscale*, 2019, **11**, 1021–1028.
35 F. Tan, W. Xu, X. Hu, P. Yu and W. Zhang, *Nanoscale Res. Lett.*, 2017, **12**, 614.
36 Y. Li, C. Feng, H. Cheng and Z. S. Wang, *Sol. RRL*, 2018, **2**, 1800222.
37 Q. Li, J. Bai, T. Zhang, C. Nie, J. Duan and Q. Tang, *Chem. Commun.*, 2018, **54**, 9575–9578.
38 J.-W. Xiao, S. Ma, S. Yu, C. Zhou, P. Liu, Y. Chen, H. Zhou, Y. Li and Q. Chen, *Nano Energy*, 2018, **46**, 45–53.
39 M. N. Lintangpradipto, N. Tsevtkov, B. C. Moon and J. K. Kang, *Nanoscale*, 2017, **9**, 10075–10083.

40 J. Qi, H. Xiong, G. Wang, H. Xie, W. Jia, Q. Zhang, Y. Li and H. Wang, *J. Power Sources*, 2018, **376**, 46–54.
41 J. Tirado, C. Roldán-Carmona, F. A. Muñoz-Guerrero, G. Bonilla-Arboleda, M. Ralaiarisoa, G. Grancini, V. I. E. Queloz, N. Koch, M. K. Nazeeruddin and F. Jaramillo, *Appl. Surf. Sci.*, 2019, **478**, 607–614.
42 L. Najafi, B. Taheri, B. Martín-García, S. Bellani, D. Di Girolamo, A. Agresti, R. Oropesa-Nuñez, S. Pescetelli, L. Vesce, E. Calabrò, M. Prato, A. E. Del Rio Castillo, A. Di Carlo and F. Bonaccorso, *ACS Nano*, 2018, **12**, 10736–10754.
43 C. Liu, M. Hu, X. Zhou, J. Wu, L. Zhang, W. Kong, X. Li, X. Zhao, S. Dai, B. Xu and C. Cheng, *NPG Asia Mater.*, 2018, **10**, 552–561.
44 S. Chen, S. Yang, H. Sun, L. Zhang, J. Peng, Z. Liang and Z.-S. Wang, *J. Power Sources*, 2017, **353**, 123–130.
45 F. Tan, W. Xu, X. Hu, P. Yu and W. Zhang, *Nanoscale Res. Lett.*, 2017, **12**, 614.
46 W. Chen, L. Xu, X. Feng, J. Jie and Z. He, *Adv. Mater.*, 2017, **29**, 1603923.
47 W. Chen, Y. Wu, J. Fan, A. B. Djurišić, F. Liu, H. W. Tam, A. Ng, C. Surya, W. K. Chan, D. Wang and Z.-B. He, *Adv. Energy Mater.*, 2018, **8**, 1703519.
48 Z. Ning, X. Gong, R. Comin, G. Walters, F. Fan, O. Voznyy, E. Yassitepe, A. Buin, S. Hoogland and E. H. Sargent, *Nature*, 2015, **523**, 324–328.
49 M. Liu, Y. Chen, C. S. Tan, R. Quintero-Bermudez, A. H. Proppe, R. Munir, H. Tan, O. Voznyy, B. Scheffel, G. Walters, A. P. T. Kam, B. Sun, M. J. Choi, S. Hoogland, A. Amassian, S. O. Kelley, F. P. Garcia de Arquer and E. H. Sargent, *Nature*, 2019, **570**, 96–101.
50 A. R. Kirmani, A. Kiani, M. M. Said, O. Voznyy, N. Wehbe, G. Walters, S. Barlow, E. H. Sargent, S. R. Marder and A. Amassian, *ACS Energy Lett.*, 2016, **1**, 922–930.
51 S. Singh and D. Kabra, *J. Mater. Chem. C*, 2018, **6**, 12052–12061.
52 A. Goel, J. B. Howard and J. B. Vander Sande, *Carbon*, 2004, **42**, 1907–1915.
53 S. Adjokatse, J. Kardula, H.-H. Fang, S. Shao, G. H. ten Brink and M. A. Loi, *Adv. Mater. Interfaces*, 2019, **6**, 1801667.
54 M. Wang, B. Li, J. Yuan, F. Huang, G. Cao and J. Tian, *ACS Appl. Mater. Interfaces*, 2018, **10**, 37005–37013.
55 W. Chen, K. Li, Y. Wang, X. Feng, Z. Liao, Q. Su, X. Lin and Z. He, *J. Phys. Chem. Lett.*, 2017, **8**, 591–598.
56 Q. Wang, Y. Shao, Q. Dong, Z. Xiao, Y. Yuan and J. Huang, *Energy Environ. Sci.*, 2014, **7**, 2359.
57 J.-W. Lee, D.-H. Kim, H.-S. Kim, S.-W. Seo, S. M. Cho and N.-G. Park, *Adv. Energy Mater.*, 2015, **5**, 1501310.
58 W. A. Laban and L. Etgar, *Energy Environ. Sci.*, 2013, **6**, 3249.
59 S. Akin, Y. Altintas, E. Mutlugun and S. Sonmezoglu, *Nano Energy*, 2019, **60**, 557–566.